Preprint Title	MHD Stagnation Point Casson Nanofluid Flow over a Radially Stretching sheet
Authors	G. Narender, K. Govardhan and G. Sreedhar Sarma
Publication Date	31 Okt 2019
Article Type	Full Research Paper
ORCID® iDs	G. Narender - https://orcid.org/0000-0003-1537-3793

MHD Stagnation Point Casson Nanofluid Flow over a Radially Stretching sheet

G. Narender[1*], K. Govardhan[2] and G. Sreedhar Sarma [1]

[1]CVR College of Engineering, Hyderabad, Telangana State, India.
[2] GITAM University, Hyderabad Campus, Telangana State, India.

* Corresponding author: gnriimc@gmail.com

Abstract

This article proposes the numerical model to investigate the impact of the radiation effects in the presence of heat generation/absorption and the magnetic field on the magnetohydrodynamics (MHD) stagnation point flow past a radially stretching sheet using the Casson nanofluid. The non-linear partial differential equations describing the proposed flow problem are reduced to a set of ordinary differential equations (ODEs) via suitable similarity transformations. The shooting technique has been used to obtain the numerical results with the help of the computational program language FORTRAN. The effects of pertinent flow parameters on the non-dimensional velocity, temperature and concentration profiles are presented in tables and graphs. From the results, it has been remarked that the heat transfer rate escalates for the larger values of the radiation parameter for the Casson nanofluid.

Keywords: Casson nanofluid, thermal radiation, MHD, Stagnation point, Nanoparticles.

1. Introduction

Heat transfer mechanism has been known for its great importance in many engineering and medical sciences for last many decades. Due to enormous benefits of heat energy for mankind, the field of thermodynamics is effectively linked with other disciplines. Heat transport process is imparting its noteworthy role in building designing [1], fuel filling system [2], air compressor [3], food industry [4], and in many other fields. In this regard fluid dynamics is playing an important role in thermal energy management by the usage of different fluids having good thermophysical properties. Researchers are emphasizing on different factors which are important for the augmentation of thermal process like involvement of porous medium, open and close cavities, implementation of magnetic effects, nanofluids, micro sized channel, etc., to enhance the thermal convection process. Choi in [5] has used the term nanofluid for the first time, which is the colloidal mixture of nanoparticles and base fluid. Most of the research has shown that metallic particles transfer more heat energy as compared to non-metallic particles.

Casson fluid, being non-Newtonian in nature, exhibits behavior of elastic solids. When stress rate is zero, the Casson fluid can be regarded as a shear thinning liquid, showing an infinite viscosity whereas the viscosity drops to zero as the stress rate approaches to an infinite value [6]. Jam, tomato ketchup, honey and concentrated fruit syrups are some familiar examples of the Casson fluid. The Casson fluid has been implemented in the preparation of printing ink, silicon suspensions and polymers [7]. During the past few years, a vast range of experiments and investigations have been carried out using the Casson fluid due to its enormous applications in the scientific and engineering domains. Dash et al. [6] examined the flow using a homogeneous porous medium inside a pipe for the Casson fluid. The stagnation point flow for mixed convection and convective boundary conditions using the Casson fluid was analyzed

by Hayat et al. [8]. Further to this, Mukhopadhyay et al. [9] investigated the flow past an unsteady stretching surface using the Casson fluid. Moreover, different aspects of such flows using the Casson fluid are presented in the recent studies [10-14].

The area of the magnetic properties of electrically conducting fluids is called Magnetohydrodynamics (MHD). Megantic fluids, liquids, metals, salt, water and electrolytes are the examples of MHD. Hannes Alfen introduced the word MHD. MHD is the sequence of Navier -stokes equations and Maxwell equations of electromagnetism is discussed by Chakraborty et al. [15]. Shah et al. [16] discussed the MHD effects and heat transfer for the UCM fluid along with Joule heating and thermal radiation using the Cattaneo-Christov heat flux model. Hayat et al. [17] clarified the mass exchange and MHD flow of an upper convected Maxwell fluid with an extended sheet. Ibrahim and Suneetha [18] studied the effects of Joule heating and viscous dissipation on steady MHD Marangoni convective flow over a at surface in the presence of radiation.

The point in the flow field where the fluid's velocity is zero is called stagnation point. The study of viscous, incompressible, fluid past a permeable plate or sheet has great importance in the field of fluid dynamics. During the past few decades, the work on stagnation point ow of an incompressible fluid past a permeable sheet has got significant importance because of its large number of applications in manufacturing industries. Some of the main applications are refrigeration of electrical gadgets by fan, atomic receptacles cooling for the duration of emergency power cut, solar receiver, etc. The study of two-dimensional (2D) stagnation point ow was first investigated by Hiemenz [19], whereas for getting the accurate solution, Eckert [20] extended this problem by adding the energy equation. In view of that Mahapatra and Gupta [21], Ishak et al. [22], and Hayat et al. [23] have studied the effcts of heat transfer in stagnation point over a permeable plate.

Moreover, an analysis of the flow using the radially stretching surfaces for the nanofluids, has many significant applications in the industrial sectors, for instance, drawing of plastic films, manufacturing of glass, production of paper and refining of crude oil. In addition to this, the implementation of the nanotechnology has been an aim of the recent analysis by many scholars because the nanoparticles exhibit remarkable electrical, optical, chemical behavior and due to their Brownian motion and thermophoresis properties. Owing to such features, the nanoparticles are widely used in catalysis, imaging, energy-based research, microelectronics, medical and environmental applications. These particles are composed of metals or non-metals. On top of that, latest investigations have made the infusion of nanoparticles, practicable in heat transfer fluids most notably water, diethylene glycol and propylene glycol to convert them into a more efficient category of heat transfer fluids [5].

Motivated by the formerly findings on the non-Newtonian and Newtonian fluids, the study of stagnation point MHD flow using the Casson nanofluids has been presented. The governing PDEs have been converted to a set of ODES through suitable similarity transformations and the numerical solution has been derived by the shooting method.

2. Mathematical Modelling

The present model aims to investigate the laminar, incompressible and steady flow of the Casson nanofluid past a radially stretched surface in proximity of a stagnation point. In the light of thermal radiation and heat generation/absorption, the characteristics of ow and heat transfer are examined. The coordinate system is chosen in a manner that $r-$ axis is along the flow whereas $z-$ axis is perpendicular to the flow.

The velocity of the outer flow is taken as U_e. Furthermore, the direction of the uniform magnetic field is chosen in such a manner that it is normal to the surface of the fluid flow. The effects of Brownian motion and thermophoresis have been elaborated. Moreover, the convective surface conditions have been taken into consideration. The constitutive equations of the Casson nanofluid model are as follow [10-14]

$$\frac{\partial u}{\partial r}+\frac{u}{r}+\frac{\partial w}{\partial z}=0, \tag{1}$$

$$\frac{\partial u}{\partial r}u+\frac{\partial v}{\partial z}w=-\frac{\sigma B_0}{\rho_f}\left(u-U_e\right)+\nu_f\left(1+\frac{1}{\beta}\right)\left(\frac{\partial^2 u}{\partial r^2}+\frac{\partial^2 u}{\partial z^2}\right), \tag{2}$$

$$\frac{\partial T}{\partial r}u+\frac{\partial T}{\partial z}w=-\frac{\nu_f}{\rho_p}\left(1+\frac{1}{\beta}\right)\left(\frac{\partial u}{\partial z}\right)^2+\alpha_f\left(\frac{\partial^2 T}{\partial r^2}+\frac{\partial^2 T}{\partial z^2}\right)-\frac{1}{\left(\rho c_p\right)_f}\frac{\partial q_r}{\partial z}+$$

$$\tau\left\{D_B\left(\frac{\partial C}{\partial z}\frac{\partial T}{\partial z}+\frac{\partial C}{\partial r}\frac{\partial T}{\partial r}\right)+\frac{D_T}{T_\infty}\left(\frac{\partial T}{\partial r}\right)^2+\left(\frac{\partial T}{\partial z}\right)^2\right\}+\frac{Q_0}{\left(\rho c_p\right)_f}\left(T-T_\infty\right)+ \tag{3}$$

$$\frac{\sigma B_0^2\left(u-U_e\right)^2}{\left(\rho c_p\right)_f},$$

$$\frac{\partial C}{\partial r}u+\frac{\partial C}{\partial z}w=D_B\left(\frac{\partial^2 C}{\partial r^2}+\frac{\partial^2 C}{\partial z^2}\right)-\frac{D_T}{T_\infty}\left(\frac{\partial^2 T}{\partial r^2}+\frac{\partial^2 T}{\partial z^2}\right)-C_r\left(C-C_\infty\right). \tag{4}$$

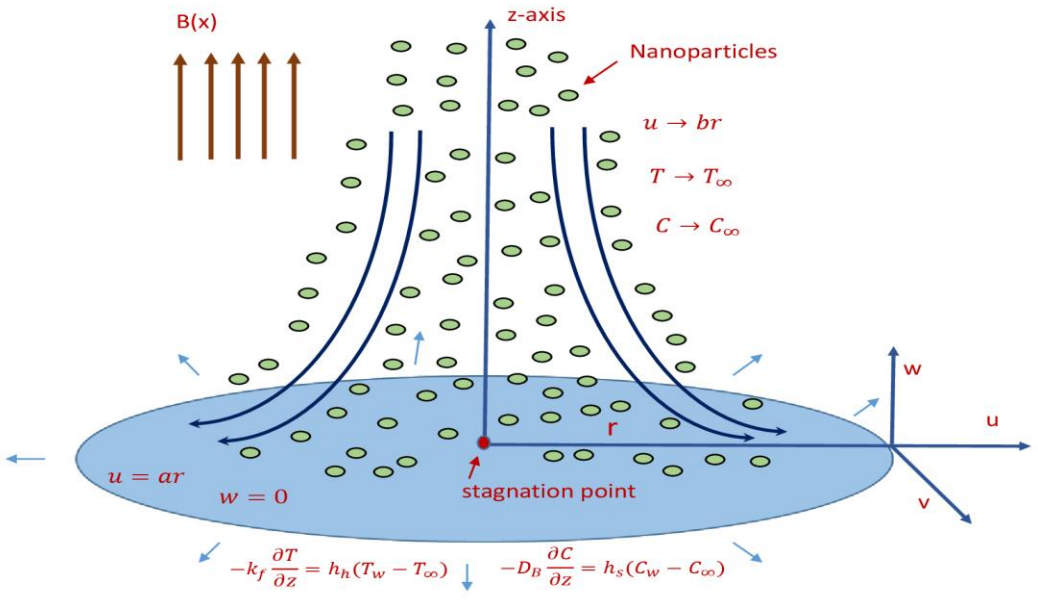

Figure 2.1: Schematic of physical model

The corresponding boundary conditions at the boundary surface are

$$u = U_w(x) = ar, w = 0, -k_f \frac{\partial T}{\partial z} = h_h\left(T_f - T\right), -D_B \frac{\partial C}{\partial z} = h_s\left(C_f - C\right) \text{ at } z = 0 \tag{5a}$$

$$u \to U_e = br, T \to T_\infty, C \to C_\infty \text{ as } z \to \infty \tag{5b}$$

The following similarity variables are taken into consideration.

$$\eta = z\sqrt{\frac{a}{\nu_f}}, u = arf'(\eta), w = -2\sqrt{a\nu_f}\, f(\eta), \theta(\eta) = \frac{T - T_\infty}{T_f - T_\infty}, \phi(\eta) = \frac{C - C_\infty}{C_w - C_\infty}.$$

The Rosseland approximation has been considered for radiation and the formulae for the radiative heat flux q_r is stated below.

$$q_r = \frac{-4\sigma^*}{3k^*}\frac{\partial T^4}{\partial z} \tag{6}$$

For smaller value of temperature contrast, the temperature difference T^4 might be expanded about T_∞ using Taylor series, as follows:

$$T^4 = T_\infty^4 + \frac{4T_\infty^3}{1!}\left(T - T_\infty\right) + \frac{12T_\infty^2}{2!}\left(T - T_\infty\right)^2 + \frac{24T_\infty^3}{3!}\left(T - T_\infty\right)^3 + ...$$

omitting the terms having higher order, we get

$$T^4 = 4T_\infty^3 T - 3T_\infty^4.$$

Then

$$\Rightarrow \frac{\partial T^4}{\partial z} = 4T_\infty^3 \frac{\partial T}{\partial z} \tag{7}$$

Using Eq. (7) in Eq. (6) and differentiating, we have the following form:

$$\frac{\partial q_r}{\partial z} = -\frac{16\sigma^* T_\infty^3}{3k^*}\frac{\partial^2 T}{\partial z^2}, \tag{8}$$

Finally, the ODEs describing the proposed flow problem can be re-collected in the following system.

$$\left(1 + \frac{1}{\beta}\right) f''' + 2ff'' - \left(f'\right)^2 + A^2 - M^2\left(f' - A\right) = 0, \tag{9}$$

$$\left(1 + \frac{4}{3}R\right)\theta'' + \Pr\left(\begin{array}{l} f\theta' + Nb\phi'\theta' + Nt\left(\theta^1\right)^2 + \left(1 + \frac{1}{\beta}\right)Ec\left(f''\right)^2 + \\ Q\theta + EcM^2\left(f' - A\right)^2 \end{array}\right) = 0, \tag{10}$$

$$\phi'' + Sc\left(2f\phi' - \gamma\phi\right) + \frac{Nt}{Nb}\theta'' = 0. \tag{11}$$

The transformed boundary conditions are stated below.

$$\left.\begin{array}{l} f(0)=0,\ f'(0)=1,\theta'(0)=-Bi_1\left[1-\theta(0)\right],\phi'(0)=-Bi_2\left[1-\phi(0)\right] at\ y=0 \\ f'(\infty)\to A,\theta(\infty)\to 0,\phi(\infty)\to 0\ as\ \eta\to\infty \end{array}\right\} \quad (12)$$

The dimensionless parameters are defined as

$$\left.\begin{array}{l} Nb=\dfrac{\tau D_B\left(C_f-C_\infty\right)}{\nu_f},\Pr=\dfrac{\nu_f}{\alpha},Nt=\dfrac{\tau D_T\left(T_f-T_\infty\right)}{\nu_f T_\infty},M^2=\dfrac{\sigma B_0^2}{\rho a}, \\ Q=\dfrac{Q_0}{\rho c_p a},R=\dfrac{4T_\infty\sigma^*}{k^*\left(\alpha\rho c_p\right)},Ec=\dfrac{a^2r^2}{\alpha c_p\left(T_f-T_\infty\right)},A=\dfrac{b}{a},Sc=\dfrac{\nu_f}{D_B}, \\ .\gamma=\dfrac{C_r}{a},Bi1=\dfrac{h_h}{k_f}\sqrt{\dfrac{\nu_f}{a}},Bi2=\dfrac{h_s}{D_B}\sqrt{\dfrac{\nu_f}{a}}. \end{array}\right\} \quad (13)$$

The formulae for the dimensional form of skin-friction coefficient, Nusselt number and Sherwood number are as follows:

$$C_f=\frac{\tau_w}{\rho_f U_w^2},Nu=\frac{rq_w}{k_f\left(T_f-T_\infty\right)},Sh=\frac{rq_w}{D_B\left(\phi_f-\phi_\infty\right)} \quad (14)$$

Given below are the formulae for τ_w, q_w and q_m.

$$\tau_w=\mu\left(1+\frac{1}{\beta}\right)\left(\frac{\partial u}{\partial z}\right)_{z=0},q_w=-k_f\left(\frac{\partial T}{\partial z}-\frac{q_r}{k_f}\right)_{z=0},q_m=-D_B\left(\frac{\partial C}{\partial z}\right)_{z=0} \quad (15)$$

The transformation of the above formulae into the dimensionless form has been carried out as:

$$C_f\sqrt{\mathrm{Re}}=\left(1+\frac{1}{\beta}\right)f''(0),\frac{Nu}{\sqrt{\mathrm{Re}}}=-\left[1+\frac{4}{3}R\right]-\theta'(0),\frac{Sh}{\sqrt{\mathrm{Re}}}-\phi'(0) \quad (16)$$

where, $\mathrm{Re}=\dfrac{rU_w}{\nu_f}$ elucidates the local Reynolds number and $\nu_f=\dfrac{\mu}{\rho}$ the kinematic viscosity.

3. Solution Methodology

In order to solve the system of ODEs (9)-(11) subject to the boundary conditions (12), the shooting technique has been used. Primarily equation (9) is solved numerically and then the computed results of f, f' and f'' are used in equations (10)-(11). For the numerical treatment of equation (9), the missing initial condition $f''(0)$ has been denoted as s and the following notations have been considered.

$$f=h_1,f'=h_2,f''=h_3,\frac{\partial f}{\partial s}=h_4,\frac{\partial f'}{\partial s}=h_5,\frac{\partial f''}{\partial s}=h_6. \quad (17)$$

Using the above notations, equation (9) can be converted into a system of three first order ODEs. First three of the following ODEs correspond to (9) and the other three are obtained by differentiating the first three w.r.t η.

$$h_1' = h_2, \qquad h_1(0) = 0,$$

$$h_2' = h_3, \qquad h_2(0) = 1,$$

$$h_3' = \frac{\beta}{1+\beta}\left[h_2^2 + M^2(h_2 - A) - 2h_1h_3 - A^2\right], \qquad h_3(0) = s,$$

$$h_4' = h_5, \qquad h_4(0) = 0,$$

$$h_5' = h_6, \qquad h_5(0) = 0,$$

$$h_6' = \frac{\beta}{1+\beta}\left[\left(2h_2 + M^2\right)h_5 - 2\left(h_1h_6 + h_3h_4\right)\right], \qquad h_6(0) = 1.$$

The Adams – Bashforth Moulton method has been used to solve the above initial value problem. In order to get the approximate numerical results, the problem's domain is bounded i.e. $[0, \eta_\infty]$, where η_∞ is chosen to be an appropriate finite positive real number in such a way that the variation in the solution for $\eta > \eta_\infty$ is ignorable. The missing condition for the above system of equations is to be chosen such that $\left(h_2(\eta_\infty)\right)_s = A$. This algebraic equation has been solved by using the Newton's method governed by the following iterative formula.

$$s^{(n+1)} = s^{(n)} - \frac{\left(h_2(\eta_\infty)\right)_{s=s^{(n)}} - A}{\left(\frac{\partial h_2(\eta_\infty)}{\partial s}\right)_{s=s^{(n)}}} \Rightarrow s^{(n+1)} = s^{(n)} - \frac{\left(h_2(\eta_\infty)\right)_{s=s^{(n)}} - A}{\left(h_5(\eta_\infty)\right)_{s=s^{(n)}}}. \tag{18}$$

The stopping criteria for the shooting method is set as

$$\left|\left(h_2(\eta_\infty)\right)_{s=s^{(n)}} - A\right| < \varepsilon, \tag{19}$$

for some very small positive number ε.

Now to solve equations (10) and (11) numerically, the missing initial conditions $\theta(0)$ and $\phi(0)$ have been denoted by l and m, respectively. Thereby the following notations have been taken into account.

$$\left.\begin{aligned} &\theta = y_1, \theta' = y_2, \phi' = y_3, \phi'' = y_4, \frac{\partial\theta}{\partial l} = y_5, \frac{\partial\theta'}{\partial l} = y_6, \frac{\partial\phi}{\partial l} = y_7 \\ &\frac{\partial\phi'}{\partial l} = y_8, \frac{\partial\theta}{\partial m} = y_9, \frac{\partial\theta'}{\partial m} = y_{10}, \frac{\partial\phi}{\partial m} = y_{11}, \frac{\partial\phi'}{\partial m} = y_{12}. \end{aligned}\right\} \tag{20}$$

Incorporating the above notations, a system of first order ODEs is achieved that is stated below.

$$y_1' = y_2, \qquad y_1(0) = l,$$

$$y_2' = \frac{-3}{3+4R}\left(\begin{array}{l}\Pr Nby_2y_4 + \Pr Nty_2^2 + 2\Pr h_1y_2 + \Pr Qy_1 \\ +\left(1+\frac{1}{\beta}\right)\Pr Ech_3^2 + +\Pr EcM^2\left(h_2 - A\right)^2\end{array}\right), \qquad y_2(0) = -Bi_1(1-l),$$

$$y_3' = y_4, \qquad y_3(0) = m,$$

$$y_4' = -\left(\frac{Nt}{Nb}\right)y_2' - Sc\left(2h_1y_4 - \gamma y_3\right), \qquad y_4(0) = -Bi_2(1-m),$$

$$y_5' = y_6, \qquad y_5(0) = 1,$$

$$y_6' = \frac{-3\Pr}{3+4R}\left(\left(Nby_4 + 2Nty_2 + 2h_1\right)y_6 + Nby_2y_8 + By_5\right), \qquad y_6(0) = Bi_1,$$

$$y_7' = y_8, \qquad y_7(0) = 0,$$

$$y_8' = \frac{3Nt\Pr}{Nb(3+4R)}\left(\begin{array}{l}\left(Nby_4 + 2Nty_2 + 2h_1\right)y_6 + By_5 + Nby_2y_8 - 2Sch_1y_8 \\ +Sc\gamma y_7\end{array}\right), \quad y_8(0) = 0,$$

$$y_9' = y_{10}, \qquad y_9(0) = 0,$$

$$y_{10}' = \frac{-3\Pr}{3+4R}\left(\left(Nby_4 + 2Nty_2 + 2h_1\right)y_{10} + Nby_2y_{12} + By_9\right), \qquad y_{10}(0) = 1,$$

$$y_{11}' = y_{12}. \qquad y_{11}(0) = 0,$$

$$y_{12}' = \frac{3Nt\Pr}{Nb(3+4R)}\left(\begin{array}{l}\left(Nby_4 + 2Nty_2 + 2h_1\right)y_{10} + By_9 + Nby_2y_{12} - 2Sch_1y_{12} \\ +Sc\gamma y_{11}\end{array}\right), y_{12}(0) = 0.$$

The Adams-Bashforth Moulton method has been taken into consideration for solving the above initial value problem. For the above system of equations, the missing conditions are to be chosen such that

$$\left(y_1(l,m)\right)_{\eta=\eta_\infty} = 0, \left(y_3(l,m)\right)_{\eta=\eta_\infty} = 0. \tag{21}$$

The above algebraic equations have been solved by using the Newton's method governed by the following iterative formula:

$$\begin{bmatrix} l^{(n+1)} \\ m^{(n+1)} \end{bmatrix} = \begin{bmatrix} l^{(n)} \\ m^{(n)} \end{bmatrix} - \left[\begin{bmatrix} \frac{\partial y_1(l,m)}{\partial l} & \frac{\partial y_1(l,m)}{\partial m} \\ \frac{\partial y_3(l,m)}{\partial l} & \frac{\partial y_3(l,m)}{\partial m} \end{bmatrix}^{-1} \begin{bmatrix} y_1 \\ y_3 \end{bmatrix}\right]_{\left(l^{(n)}, m^{(n)}, \eta_\infty\right)}$$

The stopping criteria for the shooting method is set as:

$$\max\left\{\left|y_1(\eta_\infty)\right|, \left|y_3(\eta_\infty)\right|\right\} < \varepsilon, \tag{22}$$

for some very small positive number ε. Throughout this chapter ε has been taken as 10^{-5} whereas η_∞ is set as 7.

4. Results and Discussion

In this section, the numerical results of skin-friction coefficient, Nusselt and Sher-wood numbers are illustrated with tables and graphs by assuming different values of pertinent flow parameters of interest. The admissible ranges of involved physical parameters are $0 \le M \le 2, 0.3 \le A \le 2.5, 0.1 \le \beta \le 1.5, 0.3 \le \Pr \le 2.0, 0.5 \le Ec \le 2.5, 0.1 \le R \le 0.5,$ $0.1 \le Q \le 0.5, 0.3 \le Sc \le 0.6, 0.1 \le \gamma \le 2.0, 0.1 \le Nt \le 2.0, 0.1 \le Nb \le 2, 0,$ $1 \le Bi1 \le 2.0, 0.1 \le Bi2 \le 2.0$

4.1 Skin-friction Coefficient, Nusselt and Sherwood Numbers

To validate the computational program language Fortran code, the results of $-f''(0)$ and $-\theta'(0)$ are reproduced for the problem discussed by Attia [24]. Tables 4.1-3.4 reflect an excellent agreement between the results computed by the present code and those already published in the relevant articles.

Table 4.5 discloses the numerical results of skin-friction coefficient along with Nusselt and Sherwood numbers for the present model in regards to a change in the values of various parameters like $\beta, M, R, A, \Pr, Q, Nb, Nt, Ec$ and Sc.

Table 4.1: Comparison of the computed values of $f''(0)$ with those given by Attia [24] when $Nt = Nb = R = Ec = Sc = 0$.

M	A	$f''(0)$		M	A	$f''(0)$	
		Attia	Present			Attia	Present
0	0.1	-1.1246	-1.1246260	2	0.1	-2.1138	-2.1137140
	0.2	-1.0556	-1.0555810		0.2	-1.9080	-1.9079860
	0.5	-0.7534	-0.7534078		0.5	-1.2456	-1.2455380
	1.0	0.0000	0 .0000000		1.0	0.0000	0.0000000
	1.1	0.1821	0.1820637		1.1	0.2691	0.2690781
	1.2	0.3735	0.3735214		1.2	0.5445	0.5445290
	1.5	1.0009	1.0008780		1.5	1.4080	01.4080270
1	0.1	-1.4334	-1.4334070	3	0.1	-2.9174	-2.9173560
	0.2	-1.3179	-1.3178900		0.2	-2.6141	-2.6140730
	0.5	-0.9002	-0.9001369		0.5	-1.6724	-1.6723740
	1.0	0.0000	0.0000000		1.0	0.0000	0.0000000
	1.1	0.2070	0.2070196		1.1	0.3494	0.3494373
	1.2	0.4004	0.4223360		1.2	0.7037	0.7037439
	1.5	1.1157	1.1156770		1.5	1.7954	1.7954280

Table 2: Comparison of the computed results of Nusselt number $-\theta'(0)$ with those given by Attia [24] when $Nt = Nb = R = Ec = Sc = 0$.

Pr	A	$-\theta'(0)$		Pr	A	$-\theta'(0)$	
		Attia	Present			Attia	Present
0.05	0.1	0.1273	0.166529400	0.5	0.1	0.4691	0.476318600
	0.2	0.1421	0.175023100		0.2	0.5223	0.526475900
	0.5	0.1845	0.201851100		0.5	0.6345	0.633877500
	1.0	0.2439	0.247389100		1.0	0.7699	0.764000400
	1.1	0.2545	0.256288100		1.1	0.7933	0.786525000
	1.2	0.2632	0.265061900		1.2	0.8136	0.808239000
	1.5	0.2919	0.290530900		1.5	0.8793	0.849610600

0.1	0.1	0.1618	0.194615100	1	0.1	0.7657	0.772774200
	0.2	0.1911	0.212448800		0.2	0.8152	0.818562500
	0.5	0.2615	0.265139300		0.5	0.9332	0.929409300
	1.0	0.3343	0.342184300		1.0	1.0888	1.077056000
	1.1	0.3581	0.355768200		1.1	1.1166	1.103455000
	1.2	0.3700	0.368815700		1.2	1.1408	1.129085000
	1.5	0.4080	0.405144700		1.5	1.2200	1.202041000

Table 3: The computed results of skin-friction coefficient, Nusselt and Sherwood numbers for $\gamma = 1, Bi1 = 0.1 = Bi2$, where $a_1 = \left(1 + \frac{1}{\beta}\right)$ and $a_2 = \left(1 + \frac{4}{3}R\right)$.

β	M	A	R	Pr	Q	Nb	Nt	Ec	Sc	$-a_1 f''(0)$	$-a_2\theta'(0)$	$-\phi'(0)$
0.5	1.0	0.1	0.1	0.7	0.1	0.5	0.1	0.1	1.2	2.485303	0.0859357	0.0939868
5.0										1.570312	0.0860365	0.0937332
10										1.503451	0.0859404	0.0937079
	1.2									2.688387	0.083406	0.0940580
	1.4									2.911371	0.0805399	0.0941407
		0.3								2.0619300	0.0913473	0.0938944
		0.5								1.5593120	0.0942490	0.0938664
			0.2							2.4853030	0.0954124	0.0939689
			0.3							2.4853030	0.1047357	0.0939546
				1.0						2.4853030	0.0871634	0.0940612
				2.0						2.4853030	0.0874003	0.0942927
					0.5					2.4853030	0.0688995	0.0944750
					0.7					2.4853030	0.1130105	0.0935984
						0.7				2.4853030	0.0858337	0.0939400
						0.8				2.4853030	0.0857826	0.0939254
							0.2			2.4853030	0.0858089	0.0941674
							0.3			2.4853030	0.0856807	0.0943550
								0.5		2.4853030	0.0366119	0.0959349
								1.0		2.4853030	-0.025837	0.0983850
									1.4	2.4853030	0.0859497	0.0944484
									1.6	2.4853030	0.0859616	0.0948187

Table 4: The computed results of skin-friction coefficient, Nusselt and Sherwood numbers for $\beta = 0.5, M = 1, A = 0.1, R = 0.1, \Pr = 0.7, Q = 0.1, Nt = 0.1, Nb = 0.5, Ec = 0.1, Sc = 1.2,$ where $a_1 = \left(1 + \frac{1}{\beta}\right)$ and $a_2 = \left(1 + \frac{4}{3}R\right)$.

γ	$Bi1$	$Bi2$	$-a_1 f''(0)$	$-a_2\theta'(0)$	$-\phi'(0)$
1.0	0.1	0.1	2.485303	0.0859357	0.0939868
1.5			2.485303	0.0859589	0 .0946673
2.0			2.485303	0.0859759	0 .0951565
	0.2		2.485303	0.1514275	0.0937815
	0.3		2.485303	0.2029085	0 .0936212
		0.2	2.485303	0.0857094	0 .1770382
		0.3	2.485303	0.0855062	0 .2509579

4.2 The Velocity, Temperature and Concentration

Figures 4.2-4.4 present the impact of the magnetic parameter on the velocity, temperature and concentration distributions. The larger estimation of M decelerate the

velocity and escalate the temperature and concentration of the fluid. This stems from the fact that an opposing force is generated by the magnetic field, generally referred as the Lorentz force, which depresses the motion of the fluid resulting in a decrement in the momentum boundary layer thickness and heightens the thermal and concentration boundary layer thickness.

Figures 4.5-4.7 are delineated to show the effect of A on the velocity, temperature and concentration distributions. An enhancement in the flow velocity has been observed for $A>1$. On the other hand, the velocity reduces for the case $A<1$. Also, both the temperature and concentration profiles decrease when A assumes the larger value. As the value of A heightens, the heat transfer from the sheet to the fluid becomes smaller and as a result, the temperature falls significantly. Furthermore, the thermal boundary layer thickness is reduced. Moreover, the concentration boundary layer thickness also shows a declining behaviour.

Figures 4.8-4.10 are framed to delineate the effect of Casson parameter on the velocity, temperature and concentration fields. The velocity profile shows an increasing trend by increasing β. Additionally, the velocity boundary layer thickness undergoes a decrement as β assumes the larger value. This stems from the fact that the plasticity of the Casson fluid increases for the smaller β and leads to an enhancement in the momentum boundary layer thickness. Also, the temperature distribution can be seen to rise for the increasing values of β. Further to this, the thermal boundary thickness is strengthened. A rise in the nanoparticle volume fraction has been observed for the higher estimation of β and the concentration boundary layer thickness is enhanced.

Figures 4.11-4.12 are framed to delineate the outcome of Pr on the temperature and concentration distributions. Since Pr is directly proportionate to the viscous diffusion rate and inversely related to the thermal diffusivity, so the thermal diffusion rate suffers a reduction for the larger estimation of Pr and subsequently, the temperature of the fluid drops significantly. Moreover, a decrement in the thermal boundary layer thickness has been noted. However, the nanoparticle volume fraction of the fluid can be remarked to escalates for the higher values of Pr. In addition to that, an increment can be seen in the concentration boundary layer thickness.

The outcome of Ec on the temperature profiles has been characterized through Figure 4.13. Physically, the Eckert number depicts the relation between the kinetic energy of the fluid particles and the boundary layer enthalpy. The kinetic energy of the fluid particles rises as Ec assumes the larger values. Hence, the temperature of the fluid climbs marginally and therefore, the associated momentum and thermal boundary layer thickness are enhanced.

Figures 4.14-4.15 elucidate the effect of the radiation parameter R and the heat generation or absorption parameter Q on the temperature distributions. Since the heat transfer climbs marginally for the higher estimation of R, thereby an increment in the temperature of the fluid and the thermal boundary layer has been noticed. However, as the value of Q rises, more heat is generated causing an increment in the temperature and the thermal boundary layer thickness. On the other hand, as the value of Q de-escalates, the heat absorbed results in a decrement in the temperature and the associated thermal boundary layer thickness.

Figures 4.16-4.17 delineate the outcome of Sc and γ on the concentration fields. The concentration of the fluid depicts a decreasing behaviour as Sc assumes the higher value. This behaviour stems from the fact that the Schmidt number and mass diffusion

rate have inverse relation, therefore, for the larger Sc, the process of the mass diffusivity slows down and thus, the concentration falls, and the concentration boundary layer thickness is reduced. Furthermore, the chemical reaction parameter also has a similar effect on the concentration profile. The larger values of result in a decrement in the chemical molecular diffusion and hence, the concentration of the fluid de-escalates, and the associated concentration boundary layer thickness is reduced.

Figures 4.18-4.19 interpret the impact of the thermophoresis parameter on the temperature and concentration distributions. Both the temperature and concentration escalate by taking larger values of Nt into account. In addition to this, an increment in the associated thermal and concentration boundary layer has been noticed.

Figures 4.20-4.21 display the influence of the Brownian motion parameter on the temperature and concentration distributions. The temperature profile climbs marginally for the larger values of Nb. This happens due to the reason that as the value of Nb rises, the movement of the nanoparticles enhances significantly which triggers the kinetic energy of the nanoparticles and eventually, the temperature enhances, and the thermal boundary layer thickness is magnified. On the other hand, the concentration of the fluid falls as Nb assumes the higher values. Also, the concentration boundary layer thickness is depressed.

The impact of the thermal Biot number on the temperature distribution and the concentration Biot number on the nanoparticle volume fraction has been portrayed by Figures 4.22-4.23. It is remarkable that the temperature can be observed as an increasing function of $Bi1$ and the concentration of the fluid also enhances as $Bi2$ heightens. Further to this, the associated thermal and concentration boundary layer thickness are enhanced.

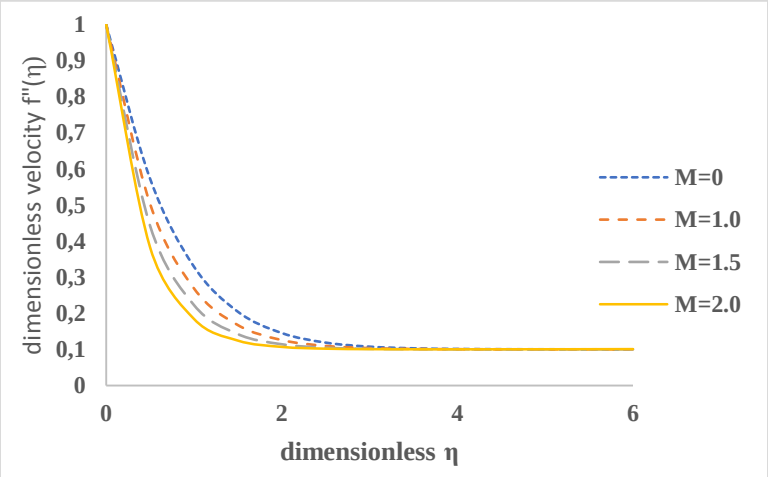

Figure 4.2. Depiction of velocity profile with increasing M.

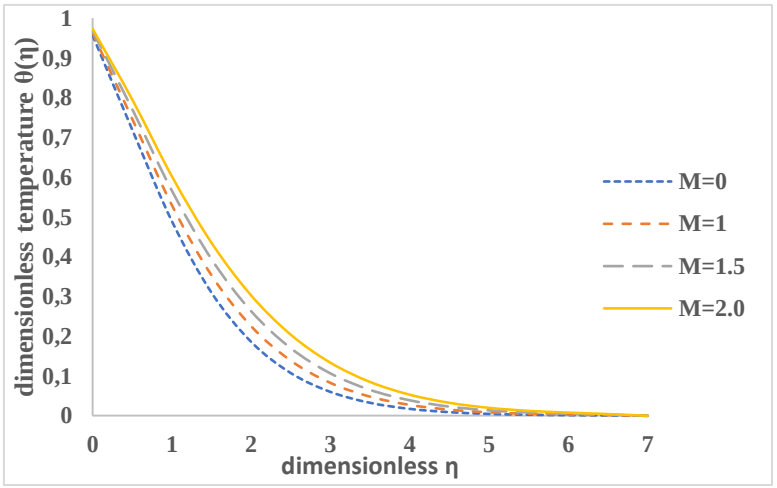

Figure 4.3. Depiction of temperature profile with increasing M

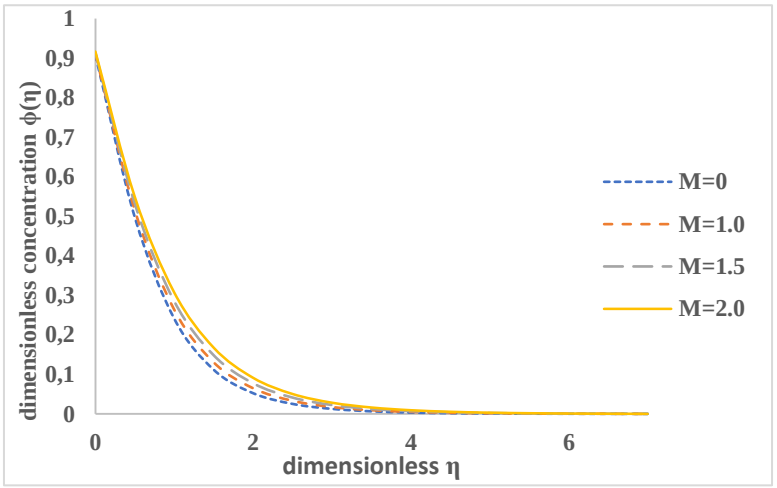

Figure 4.4. Depiction of concentration profile with increasing M

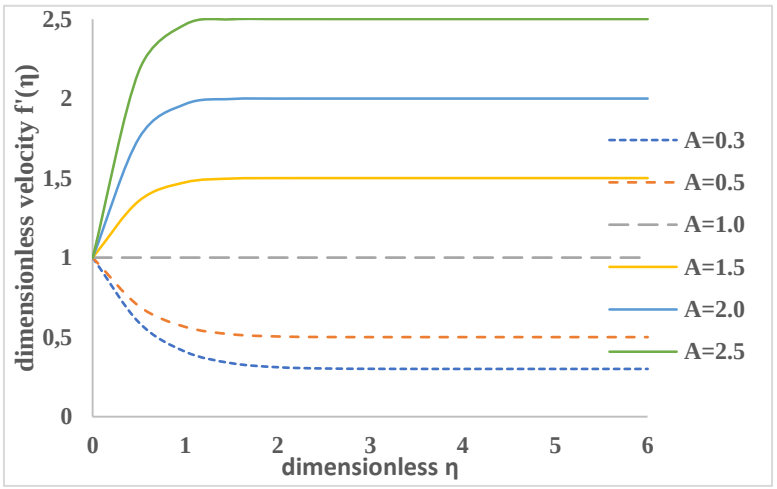

Figure 4.5. Depiction of velocity profile with increasing A

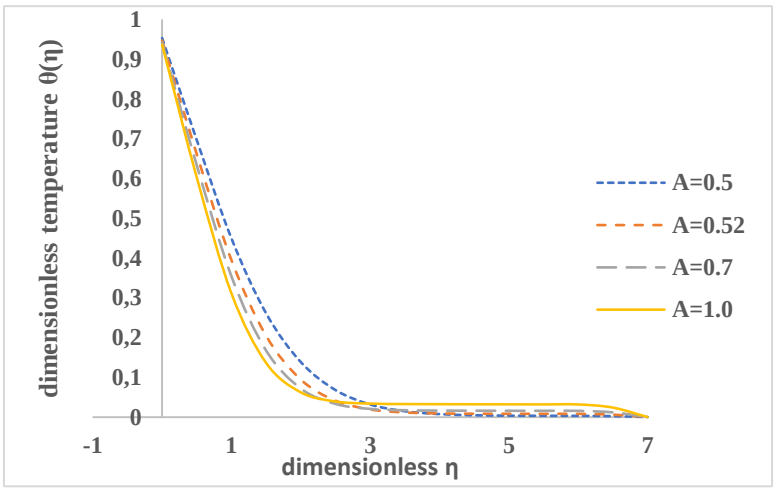

Figure 4.6. Depiction of temperature profile with increasing A

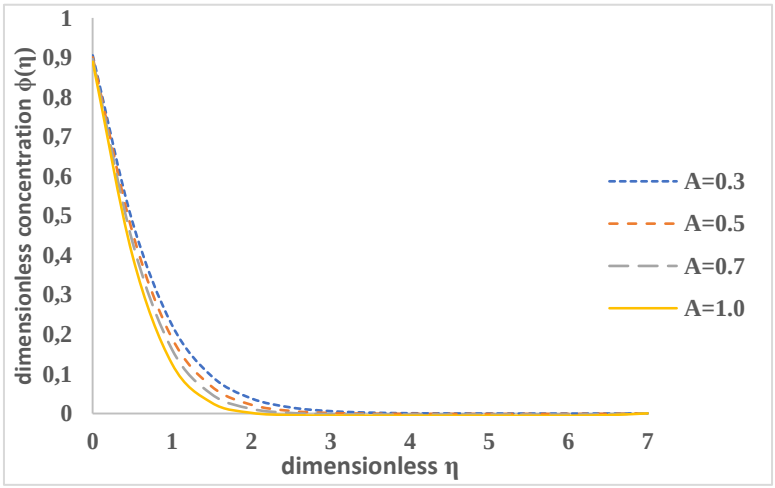

Figure 4.7. Depiction of concentration profile with increasing A

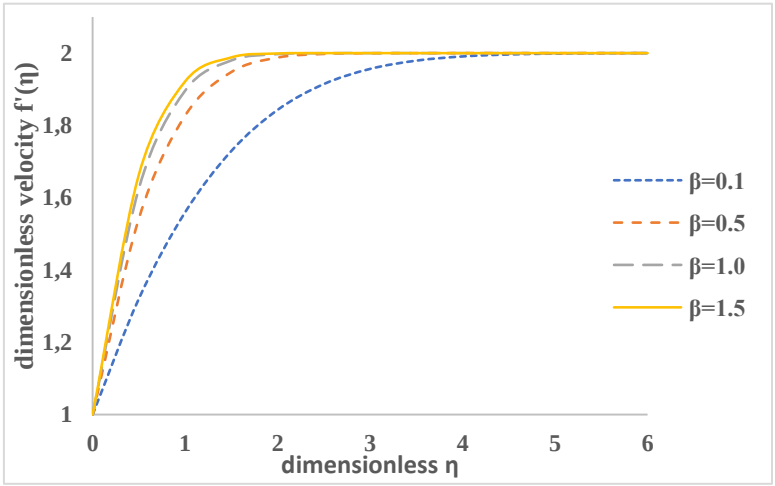

Figure 4.8. Depiction of velocity profile with increasing β

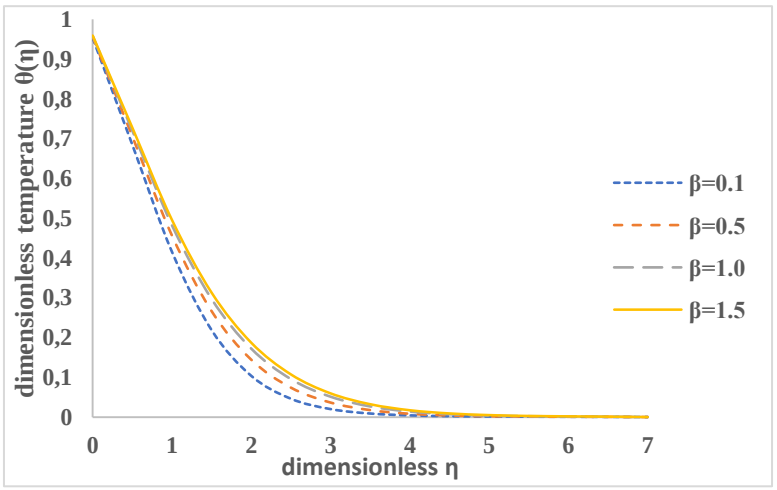

Figure 4.9. Depiction of temperature profile with increasing β

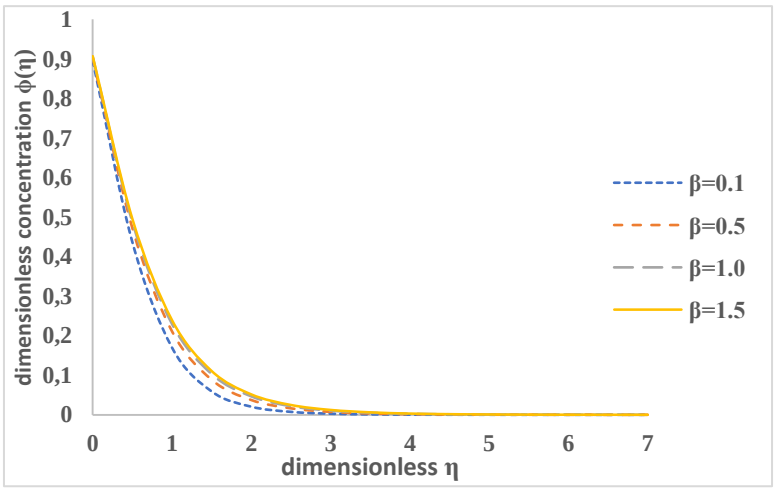

Figure 4.10. Depiction of concentration profile with increasing β

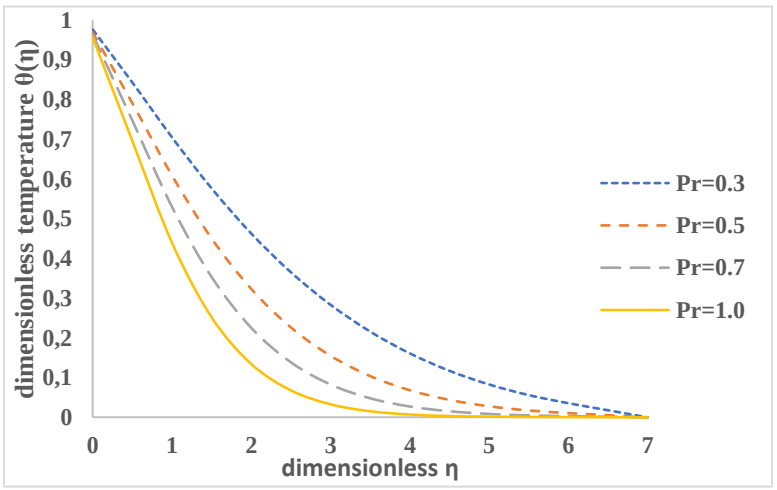

Figure 4.11. Depiction of temperature profile with increasing Pr

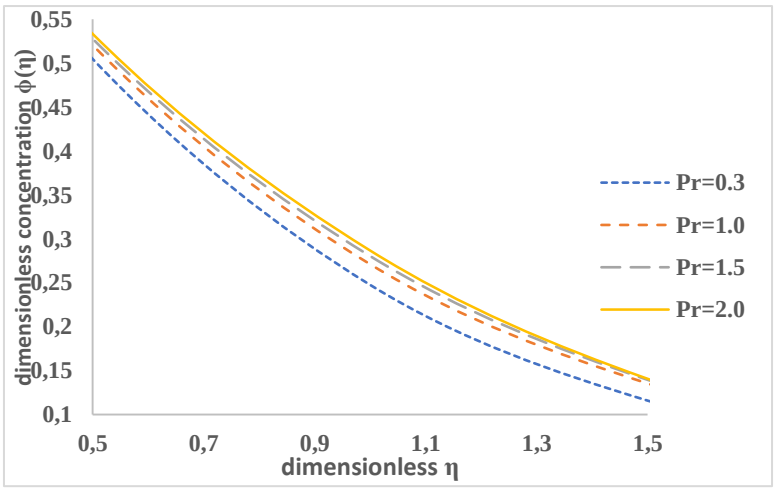

Figure 4.12. Depiction of concentration profile with increasing Pr

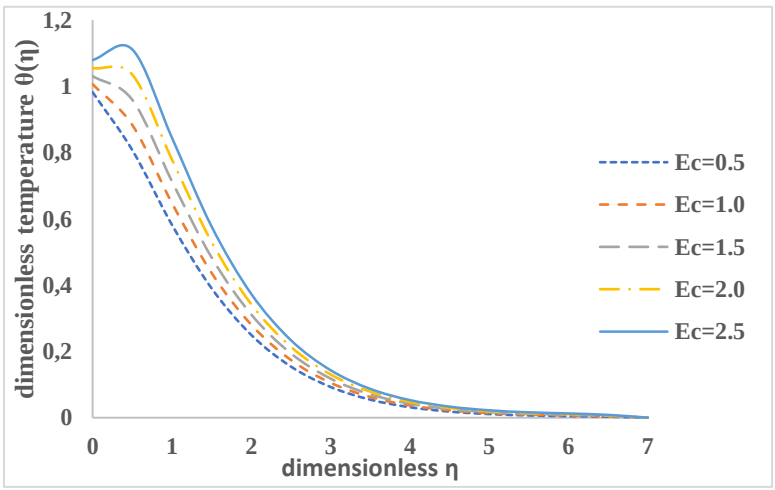

Figure 4.13. Depiction of temperature profile with increasing *Ec*

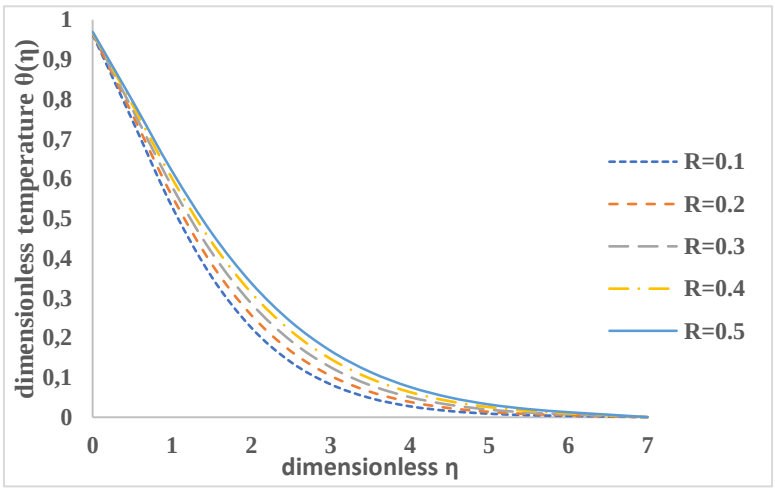

Figure 4.14. Depiction of temperature profile with increasing *R*

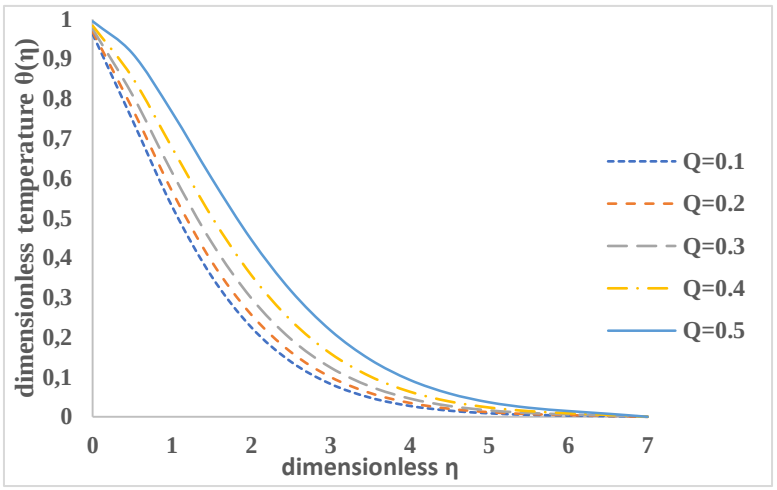

Figure 4.15. Depiction of temperature profile with increasing Q

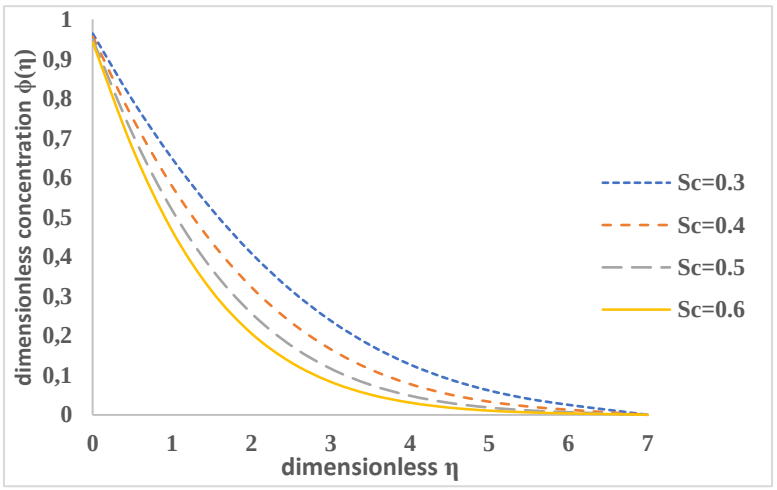

Figure 4.16. Depiction of concentration profile with increasing Sc

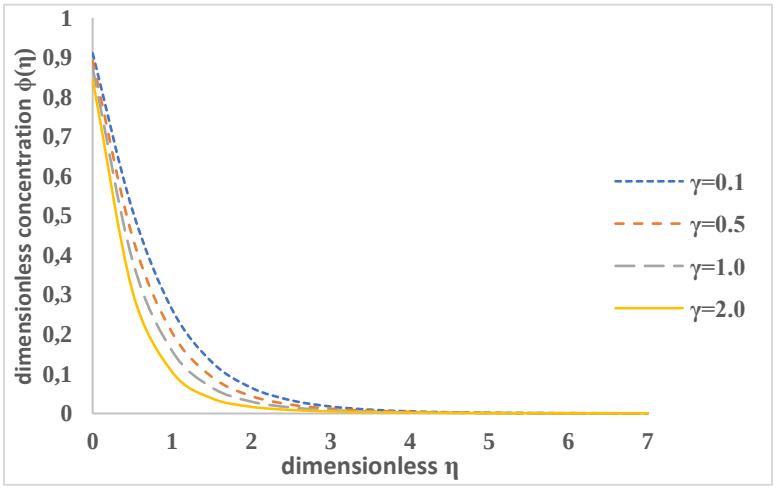

Figure 4.17. Depiction of concentration profile with increasing γ

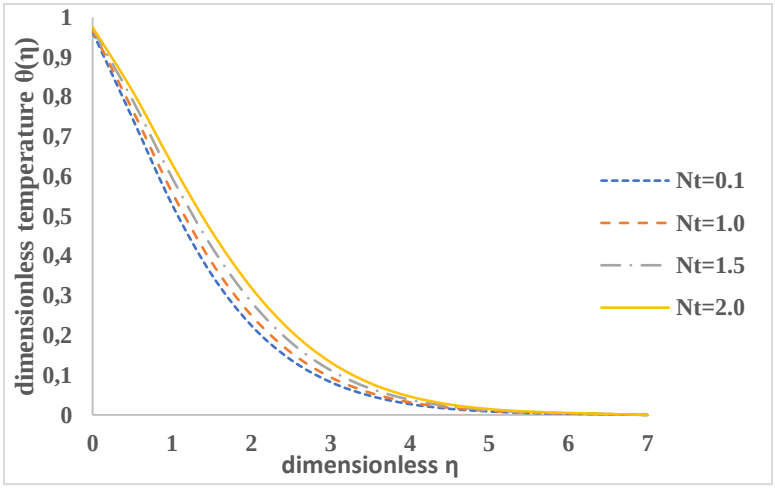

Figure 4.18. Depiction of temperature profile with increasing *Nt*

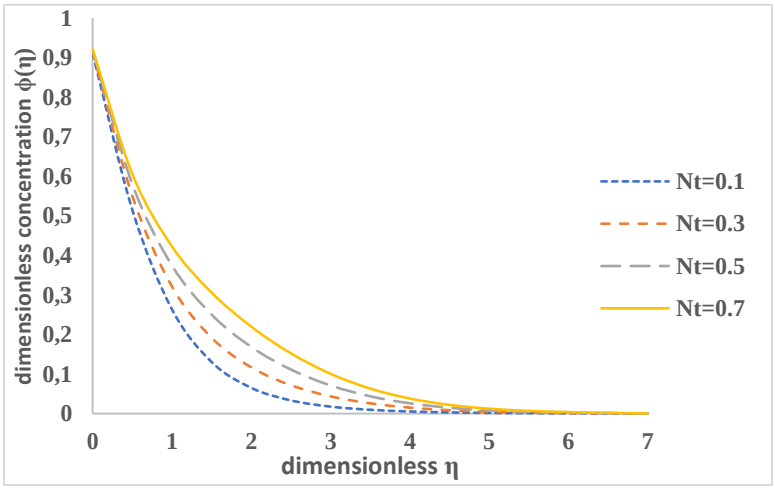

Figure 4.19. Depiction of concentration profile with increasing *Nt*

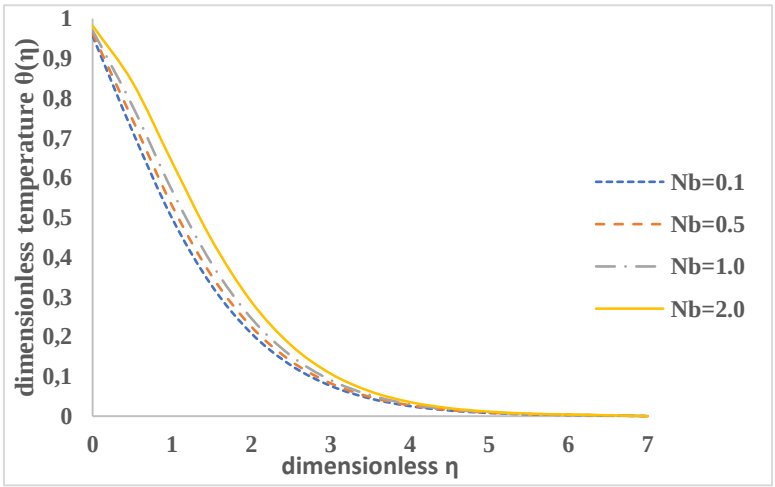

Figure 4.20. Depiction of temperature profile with increasing *Nb*

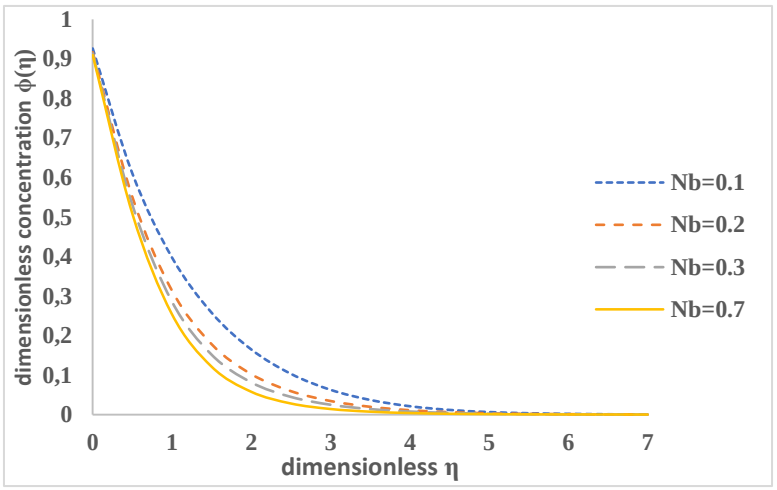

Figure 4.21. Depiction of concentration profile with increasing *Nb*

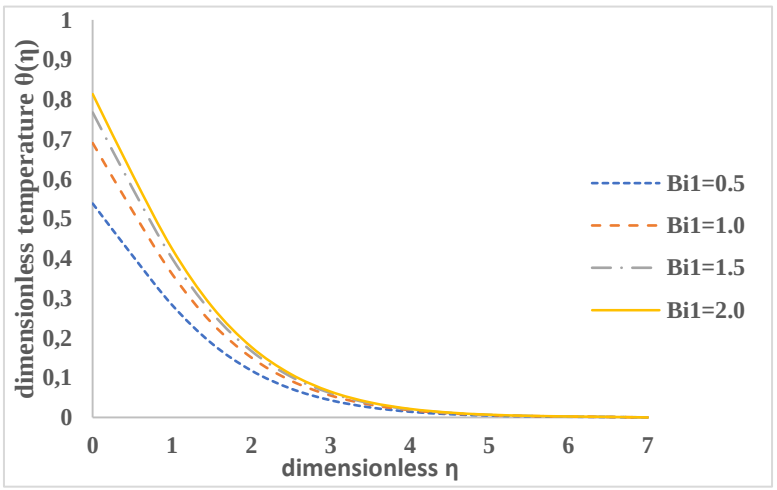

Figure 4.22. Depiction of temperature profile with increasing *Bi*1

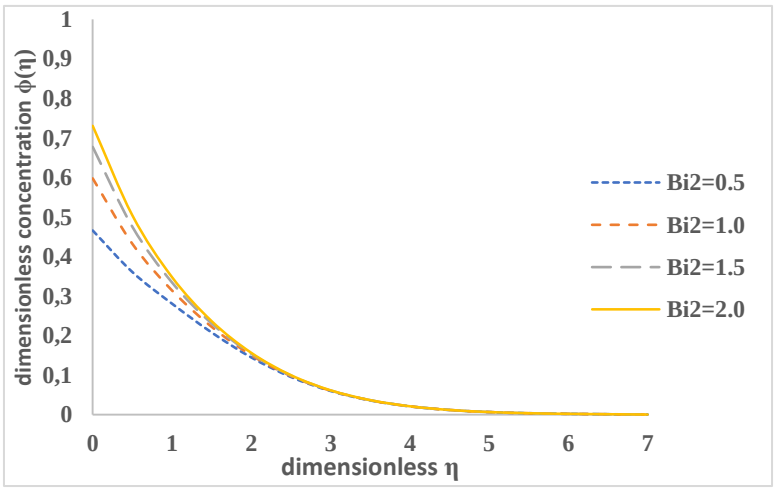

Figure 4.23. Depiction of concentration profile with increasing $Bi2$

5. Conclusion

The conclusions drawn from the numerical results are summarized below.

The magnetic parameter decelerates the velocity whereas an opposite trend has been observed for the temperature and concentration β fields by considering the Casson fluid. For the Casson fluid, the higher estimation of the Casson parameter escalates the velocity, temperature and concentration profiles. The temperature falls whereas the concentration escalates for the larger estimation of the Prandtl number in view of the Casson. The Eckert number accelerates the velocity and the temperature profile climbs marginally for the Casson fluid. The heat and mass transfer rates climb significantly as the value of thermophoresis parameter escalates, by considering the Casson fluids into account. For the Casson fluids, the heat transfer rate escalates for the radiation parameter.

References

1. Z. Zhai, "Application of computational fluid dynamics in building design: aspects and trends", Indoor and Built Environment, vol. 15, no. 4, pp. 305-313, 2006.
2. R. Banerjee, X. Bai, D. Pugh, K. Isaac, D. Klein, J. Edson, W. Breig, and L. Oliver, "CFD simulations of critical components in fuel filling systems", Tech. Rep. 2002-01-0573, SAE Technical Paper, SAE 2002 World Congress, Detroit Michigan, pp. 1-19, March 2002.
3. C. Zhang, M. Saadat, P. Y. Li, and T. W. Simon, "Heat transfer in a long, thin tube section of an air compressor: an empirical correlation from CFD and a thermodynamic modeling", in American Society of Mechanical Engineers (ASME) 2012 International Mechanical Engineering Congress and Exposition, vol. 7, (Houston Texas (USA)), pp. 1601-1607, 2012.
4. B. Xia and D. W. Sun, "Applications of computational fluid dynamics (CFD) in the food industry: a review", Computers and Electronics in Agriculture, vol. 34, no. 1-3, pp. 5-24, 2002.
5. S. U. S. Choi, "Nanofluid technology: current status and future research", Tech. Rep. ANL/ET/CP-97466, Argonne National Lab. (ANL), Argonne, IL (United States), pp. 1-21, Oct.20, 1998.
6. R. K. Dash, K. N. Mehta, and G. Jayaraman, "Casson fluid flow in a pipe filled with a homogeneous porous medium", International Journal of Engineering Science, vol. 34, no. 10, pp. 1145-1156, 1996.
7. J. Venkatesan, D. S. Sankar, K. Hemalatha, and Y. Yatim, "Mathematical analysis of Casson fluid model for blood rheology in stenosed narrow arteries", Journal of Applied Mathematics, vol. 2013, pp. 1-11, 2013.
8. T. Hayat, S. A. Shehzad, S. A. Alsaedi, and M. S. Alhothuali, "Mixed convection stagnation point flow of Casson fluid with convective boundary conditions", Chinese Physics Letters, vol. 29, no. 11, p. 114704, 2012.
9. S. Mukhopadhyay, P. R. De, K. Bhattacharyya, and G. Layek, "Casson fluid flow over an unsteady stretching surface", Ain Shams Engineering Journal, vol. 4, no. 4, pp. 933-938, 2013.

10. S. Mukhopadhyay, “Casson fluid flow and heat transfer over a nonlinearly stretching surface”, Chinese Physics B, vol. 22, no. 7, pp. 074701, 2013.
11. S. Nadeem, R. U. Haq, N. S. Akbar, and Z. Khan, “MHD three-dimensional Casson fluid flow past a porous linearly stretching sheet”, Alexandria Engineering Journal, vol. 52, no. 4, pp. 577-582, 2013.
12. A. Khalid, I. Khan, A. Khan, and S. Shafie, “Unsteady MHD free convection flow of Casson fluid past over an oscillating vertical plate embedded in a porous medium”, Engineering Science and Technology, an International Journal, vol. 18, no. 3, pp. 309-317, 2015.
13. M. I. Khan, M. Waqas, T. Hayat, and A. Alsaedi, “A comparative study of Casson fluid with homogeneous-heterogeneous reactions”, Journal of Colloid and Interface science, vol. 498, pp. 85-90, 2017.
14. Z. Shah, S. Islam, H. Ayaz, and S. Khan, “Radiative heat and mass transfer analysis of micropolar nanofluid flow of Casson fluid between two rotating parallel plates with effects of hall current," Journal of Heat Transfer, vol. 141, no. 2, pp. 022401, 2019.
15. B. K. Chakraborty and H. P. Mazumdar, “MHD flow of a Newtonian fluid over a stretching sheet: an approximate solution”, Approximation Theory and its Applications, vol. 16, no. 3, pp. 32-41, 2000.
16. S. Shah, S. Hussain, and M. Sagheer, “MHD effects and heat transfer for the UCM fluid along with Joule heating and thermal radiation using cattaneo-christov heat flux model”, AIP Advances, vol. 6, no. 8, pp. 085-103, 2016.
17. T. Hayat, Z. Abbas, and N. Ali, “MHD flow and mass transfer of an upper convected Maxwell fluid past a porous shrinking sheet with chemical reaction species”, Physics Letters A, vol. 372, no. 26, pp. 4698-4704, 2008.
18. S. M. Ibrahim and K. Suneetha, “Heat source and chemical effects on MHD convection flow embedded in a porous medium with soret, viscous and Joules dissipation”, Ain Shams Engineering Journal, vol. 7, no. 2, pp. 811-818, 2016.
19. K. Hiemenz., “Die Grenzschicht an einem in den gleichformigen Flussigkeitsstrom eingetauchten geraden Kreiszylinder”. PhD thesis, 1911.
20. E. Eckert., “Die Berechnung des Warmeubergangs in der laminaren Grenzschicht umstromter Korper. VDI-Forschunhsheft”, 1942.
21. T. R. Mahapatra and A. S. Gupta, “Heat transfer in stagnation-point ow towards a stretching sheet”, Heat and Mass transfer, vol. 38, no. 6, pp. 517-521, 2002.
22. A. Ishak, R. Nazar, and I. Pop, “Mixed convection boundary layers in the stagnation point flow towards a stretching vertical sheet”, Meccanica, vol. 41, no. 5, pp. 509-518, 2006.
23. T. Hayat, M. Mustafa, S. A. Shehzad, and S. Obaidat, “Melting heat transfer in the stagnation-point flow of an upper-convected Maxwell UCM fluid past a stretching sheet”, Int. J. Numerical Methods in Fluids, vol. 68, no. 2, pp. 233-243, 2012.
24. H. A. Attia, “Axisymmetric stagnation point ow towards a stretching surface in the presence of a uniform magnetic field with heat generation”, Tamkang J. Sci. Eng., vol. 10, no. 1, pp. 1116, 2007.